OPEN

NPG Asia Materials (2016) 8, e237; doi:10.1038/am.2015.143
www.nature.com/am

ORIGINAL ARTICLE

Organic-inorganic hybrid PtCo nanoparticle with high electrocatalytic activity and durability for oxygen reduction

Namgee Jung[1], Satadeep Bhattacharjee[2,3], Sanjeev Gautam[4], Hee-Young Park[5], Jaeyune Ryu[5], Young-Hoon Chung[5], Sang-Young Lee[5], Injoon Jang[5], Jong Hyun Jang[5], Sae Hum Park[5], Dong Young Chung[6], Yung-Eun Sung[6], Keun-Hwa Chae[7], Umesh V Waghmare[2], Seung-Cheol Lee[2,8] and Sung Jong Yoo[5]

In Pt-transition metal (TM) alloy catalysts, the electron transfer from the TM to Pt is retarded owing to the inevitable oxidation of the TM surface by oxygen. In addition, acidic electrolytes such as those employed in fuel cells accelerate the dissolution of the surface TM oxide, which leads to catalyst degradation. Herein, we propose a novel synthesis strategy that selectively modifies the electronic structure of surface Co atoms with N-containing polymers, resulting in highly active and durable PtCo nanoparticle catalysts useful for the oxygen reduction reaction (ORR). The polymer, which is functionalized on carbon black, selectively interacts with the Co precursor, resulting in Co–N bond formation on the PtCo nanoparticle surface. Electron transfer from Co to Pt in the PtCo nanoparticles modified by the polymer is enhanced by the increase in the difference in electronegativity between Pt and Co compared with that in bare PtCo nanoparticles with the TM surface oxides. In addition, the dissolution of Co and Pt is prevented by the selective passivation of surface Co atoms and the decrease in the O-binding energy of surface Pt atoms. As a result, the catalytic activity and durability of PtCo nanoparticles for the ORR are significantly improved by the electronic ensemble effects. The proposed organic/inorganic hybrid concept will provide new insights into the tuning of nanomaterials consisting of heterogeneous metallic elements for various electrochemical and chemical applications.
NPG Asia Materials (2016) **8,** e237; doi:10.1038/am.2015.143; published online 22 January 2016

INTRODUCTION

Proton exchange membrane fuel cells (PEMFCs) are promising green energy conversion devices because they convert hydrogen gas directly into electricity without emitting pollutants.[1] However, large quantities of precious Pt catalysts are required to fabricate PEMFCs with high electrochemical catalytic efficiency because the oxygen reduction reaction (ORR) at the cathode has a high overpotential, even on a Pt catalyst.[2–5] Improving the fuel cell efficiency by simply increasing the Pt loading in the cathode is difficult because the use of a thick electrode concomitantly leads to other resistances such as concentration and internal resistances.[6,7] Therefore, to simultaneously decrease the use of Pt and enhance the intrinsic catalytic activity, transition metals (TMs) have been alloyed with Pt to produce bimetallic PtM (where M = Co, Fe or Ni) catalysts, which can be used as cathode materials for fuel cells.[8–18] The TMs are incorporated into the Pt lattice during nanoparticle synthesis, which causes compressive strain in the lattice and thereby decreases the Pt lattice constant.[9–14] It is also well-known that electrons are transferred from the TMs to the Pt owing to the difference in their electronegativities. For example, Pt and Co have electronegativity values of 2.28 and 1.88, respectively. Owing to the high electronegativity difference (0.4) between them, some of the electrons in Co can transfer into the *d*-orbital of Pt, which could result in filling the Pt *d*-band and downshifting the *d*-band center energy.[9–18] As a result, the binding energy between the surface Pt and the O species (reaction intermediates such as –OOH and –OH) is weakened. These alloying effects of TMs have been described in many scientific reports using density functional theory (DFT) calculations.[1,5,13,17,19]

However, despite the development of state-of-the art synthesis methods, PtM nanoparticles that match the high ORR activities expected from theoretical calculations have not been synthesized. Furthermore, the synthesized PtM nanoparticles have exhibited variability in the absolute ORR activity values, depending on the

[1]Graduate School of Energy Science and Technology (GEST), Chungnam National University, Daejeon, Korea; [2]Indo-Korea Science and Technology Center (IKST), Korea Institute of Science and Technology (KIST), Bangalore, India; [3]Theoretical Sciences Unit and Sheikh Saqr Laboratory, Jawaharlal Nehru Center for Advanced Scientific Research (JNCASR), Bangalore, India; [4]Dr. SS Bhatnagar University Institute of Chemical Engineering & Technology, Panjab University, Chandigarh, India; [5]Fuel Cell Research Center, Korea Institute of Science and Technology (KIST), Seoul, Korea; [6]Center for Nanoparticle Research, Institute for Basic Science (IBS), School of Chemical and Biological Engineering, Seoul National University, Seoul, Korea; [7]Advanced Analysis Center, Korea Institute of Science and Technology (KIST), Seoul, Korea and [8]Electronic Materials Research Center, Korea Institute of Science and Technology (KIST), Seoul, Korea
Correspondence: Dr S-C Lee, Electronic Materials Research Center, Korea Institute of Science and Technology (KIST), Seoul 136-791, Korea.
E-mail: leesc@kist.re.kr
or Dr SJ Yoo, Fuel Cell Research Center, Korea Institute of Science and Technology, 39-1 Hawolgok-dong Wolsong-gil 5, Seoul 136sa-791, Korea.
E-mail: ysj@kist.re.kr
Received 11 February 2015; revised 24 June 2015; accepted 1 November 2015

surface structures.[1,5,12,20] Although there are various reasons for the mismatch between the practical and theoretical ORR activities, mainly stemming from the various assumptions made regarding the catalyst surface structures in the DFT calculations, we think that one of the most important issues may be the change in the Pt electronic structure caused by the TM oxides on the nanoparticle surfaces. On a real PtM nanoparticle surface, the high oxophilicity of TM atoms encourages the formation of surface oxides when the PtM alloy catalysts are fabricated by solution-based synthesis methods or when they are exposed to oxygen (or air) and water vapor in ambient air.[21–25] In fact, X-ray photoelectron spectroscopy (XPS) has confirmed that surface TM oxides with various oxidation states are produced by the interaction of the TMs with O species during the PtM nanoparticle synthesis, which affect the ORR activity of the surface Pt atoms that function as active sites.[23–25] In addition, the surface TM oxides are rapidly dissolved when the PtM nanoparticles are used as catalytic cathodes in acid electrolytes for ORR.[5,26–28] These electrochemical and chemical dealloying phenomena are widely known to be critical factors for catalyst degradation.

On the other hand, surface-dealloyed PtM nanoparticles with Pt-skeleton or Pt-skin surfaces generated through elaborate surface modification techniques have shown enhanced ORR activities compared with the activities of as-prepared PtM catalysts owing to the removal of the inactive TM oxides from the surfaces during the dealloying process.[29–34] However, the synthesis methods for Pt-skeleton and Pt-skin surfaces are very complicated and need to be performed very carefully, because they involve multiple steps such as acid and heat treatments and surface-sensitive techniques. Therefore, it would be scientifically much more useful to simultaneously control the electronic structure of the surface Pt and prevent surface TM oxide formation in a one-pot synthesis method for PtM alloy nanoparticles.

When the TM atoms on PtM nanoparticle surfaces are oxidized by O species, the electronic structures of the TMs are likely to be considerably altered by the anionic characteristics of the O species.[35,36] Because the surface TM atoms already lose many electrons to O, which has a much higher electronegativity (3.44) than Pt (2.28), the difference in the electronegativities between the Pt and TM atoms becomes small owing to the competitive electronic rearrangement among the Pt, TM and O species.[37] The lower electronegativity difference between Pt and the TM may result in a decrease in the number of electrons transferred from the TM to Pt on the PtM nanoparticle surface. Therefore, despite the great benefits of PtM alloying, the PtM nanoparticles are likely to lose their high intrinsic surface catalytic properties because the Pt receives fewer electrons from the TM atoms owing to the presence of surface O.

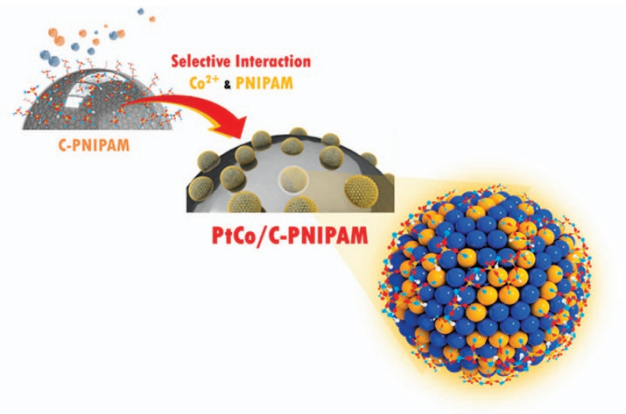

Figure 1 Schematic diagram of the surface modification of PtCo nanoparticles using C-PNIPAM. The N moieties of amide functional groups in the PNIPAM chain are expected to interact selectively with the surface Co atoms on the PtCo nanoparticles. The blue and yellow balls represent the Pt and Co atoms, respectively.

However, in practice, it is difficult to prevent the surface TM atoms from being naturally oxidized in air or acidic electrolytes without using additional blocking materials. Accordingly, to increase the electron transfer from TM to Pt, it is necessary to intentionally attach atoms such as N that have lower electronegativities (the electronegativity of N is 3.04) to the surface TM atoms instead of the highly electronegative O species.[38,39] Simultaneously, the surface Pt atoms should be selectively protected from interacting with additional materials because these atoms provide electrochemically active sites for the ORR on the surface of PtM alloy nanoparticles.

Herein, we have developed a highly active and durable carbon-supported PtCo alloy nanoparticle (PtCo/C-PNIPAM) using poly (*N*-isopropylacrylamide) (PNIPAM)-functionalized carbon (C-PNIPAM) as a support material to selectively modify the surface of the Co atoms with N moieties as shown in Figure 1. The electronic structures of Pt and Co were dramatically changed by the selective interaction of PNIPAM with Co. We measured the ORR activity and durability of the catalyst materials and compared them with traditional PtCo/C catalysts that were not modified with PNIPAM. In addition, we have elucidated the enhancements of the ORR activity and durability of the new material via DFT calculations.

MATERIALS AND METHODS

Preparation of C-PNIPAM

C-PNIPAM was prepared via the chemical reaction between carbon black (Vulcan XC-72R, Cabot, Boston, MA, USA) and amine-terminated PNIPAM (NH_2-PNIPAM, average $M_n = 5500$, Sigma-Aldrich, St Louis, MO, USA). Carbon black (0.3 g) and NH_2-PNIPAM (0.4 mmol) were mixed together in an acid solution with a pH of 1.6, which was composed of 300 ml ethanol (Sigma-Aldrich) and 0.6 ml $HClO_4$ (Sigma-Aldrich). The carbon black was dispersed in the solution by sonication for 30 min, and the solution was further stirred for 30 min at room temperature. Next, 0.4 mmol 1-ethyl-3-(3-dimethylaminopropyl)carbodiimide (EDC, Fluka) was introduced into the vigorously stirred solution to catalyze the amide reaction between the –COOH on the carbon surface and the $–NH_2$ belonging to NH_2-PNIPAM. After the amide reaction with EDC for 12 h, the solution was washed with an excess of deionized water and then filtered. The filtered C-PNIPAM was dried at 60 °C and subsequently ground in a mortar to obtain a C-PNIPAM powder.

Catalyst preparation

Catalysts with 40 wt.% PtCo/C-PNIPAM were synthesized using C-PNIPAM as a support material. After 0.15 g C-PNIPAM was dispersed in ethanol (300 ml) for 1 h, $PtCl_4$ (0.4 mmol; Sigma-Aldrich, St Louis, MO, USA), $CoCl_2{\cdot}6H_2O$ (0.4 mmol; Sigma-Aldrich) and sodium acetate (8 mmol; Sigma-Aldrich) were added into the C-PNIPAM/ethanol solution with vigorous stirring. $NaBH_4$ (Sigma-Aldrich) was then quickly introduced into the solution as a reducing agent. The resultant solution was stirred for 4 h to complete the reaction. Finally, the solution was washed with an excess of ethanol and deionized water, and the PtCo/C-PNIPAM was filtered and dried in an oven at 60 °C. In the case of PtCo/C, bare carbon black was used as the support material. PtCo/C was prepared using the same materials (except for the addition of the carbon support) and procedure as for the PtCo/C-PNIPAM. $PtCl_4$ (0.2 mmol) was used as the Pt precursor to obtain 20 wt.% Pt/C and Pt/C-PNIPAM, whereas $CoCl_2{\cdot}6H_2O$ (0.64 mmol) was used as the Co precursor for 20 wt.% Co/C and Co/C-PNIPAM. While bare carbon black served as the support material for Pt/C and Co/C, C-PNIPAM was used as the support material for Pt/C-PNIPAM and Co/C-PNIPAM. The prepared catalysts were heat treated at 200 °C for 2 h in an Ar atmosphere.

Physical characterization

To confirm the quantity of PNIPAM functionalized on the carbon surface, thermogravimetric analysis (TGA) (Q50 TGA, TA Instruments, New Castle, DE, USA) was performed at a heating rate of 10 °C min^{-1} in an air atmosphere. Ultraviolet–visible (UV–Vis) spectra of the metal precursors dissolved in ethanol were recorded by an Agilent UV–Vis-NIR (Cary 5000, Santa Clara, CA, USA) spectrophotometer. Near-edge X-ray absorption fine structure (NEXAFS) measurements for C K-, N K- and Co L-edge were performed at the 10D XAS-KIST beamline with an electron-beam energy of 3 GeV and a maximum stored current of 250 mA at the Pohang Accelerator Lab (PAL, Pohang, Korea). The NEXAFS spectra were collected in the total electron yield mode by recording the sample drain current. X-ray absorption near-edge structure (XANES) data for the Pt L_3-edge were recorded using the 8C beamline at PAL with a Si (111) double crystal monochromator. The raw data were energy calibrated (using E_0 of the Pt foil), smoothed, background-corrected and normalized using the Athena program in the IFEFFIT software package. The XPS spectra were obtained using the 8A1 beamline at PAL, and the resultant data were curve-fitted using XPSPEAK4.1 software. X-ray diffraction patterns were measured using the 9B beamline at PAL. Transmission electron microscope (TEM) images, energy-dispersive X-ray spectroscopy mapping images and line profiles of the samples were obtained by a Cs-corrected scanning TEM (STEM) (JEM-ARM200F, JEOL, Tokyo, Japan).

Electrochemical characterization

All electrochemical measurements were conducted in a standard three-compartment electrochemical cell using the glassy carbon electrode from a rotating disk electrode (RDE) setup, a Pt wire and a saturated calomel electrode (SCE) as the working, counter and reference electrodes, respectively. PtCo/C, PtCo/C-PNIPAM, Pt/C and Pt/C-PNIPAM were tested at a room temperature in 0.1 M $HClO_4$. For the Co/C and Co/C-PNIPAM samples, the electrochemical measurements were conducted at room temperature in 0.1 M KOH. All the potential values were reported versus the reversible hydrogen electrode (RHE). The RHE calibration was conducted in each solution by measuring the currents between the potential ranges for the hydrogen oxidation and evolution reactions with a Pt disk electrode. When the current at the Pt disk was zero at a certain potential value between the potential ranges for the hydrogen oxidation and evolution reactions, that potential value was defined as 0.00 V_{RHE} for each solution. We conducted the potential shift by the potential value at zero current depending on the electrolyte used. The catalyst ink slurry was prepared by mixing each catalyst with 5 wt.% Nafion solution (Sigma-Aldrich), which acted as a binding material and 2-propanol (SK Chemical, Seongnam, Korea). Following mixing and sonication, a drop of the ink slurry was applied to the glassy carbon substrate (0.196 cm^2, geometric surface area) and then dried. The dried electrode was then transferred to the electrochemical cell. Cyclic voltammograms (CVs) were obtained by cycling the potential between 0.05 V_{RHE} and 1.05 V_{RHE} at a scan rate of 20 mV s^{-1} in Ar-saturated electrolytes. During the ORR tests, the potential was scanned at a rate of 5 mV s^{-1} (from 0.05 V_{RHE} to 1.05 V_{RHE}) and a rotating speed of 1600 r.p.m. in O_2-saturated electrolytes. The accelerated durability tests (ADTs) for PtCo/C and PtCo/C-PNIPAM samples were performed by cycling the potential 5000 times at a scan rate of 100 mV s^{-1} between 0.6 V_{RHE} and 1.1 V_{RHE} in O_2-saturated 0.1 M $HClO_4$. After 5000 cycles, the CVs and ORR polarization curves of the catalysts were measured again and compared with those of the catalysts before the ADT.

Computational details

Our first-principles calculations are within the framework of DFT with the Perdew–Burke Ernzerhof exchange-correlation energy functional based on a generalized gradient approximation.[40] We used a projector augmented-wave method as implemented by the Vienna *ab initio* simulation package (VASP).[41] The (111) surfaces were modeled with supercells comprising slabs of 4×4 in-plane unit cells containing 64 atoms with a thickness of four atomic layers and a vacuum of 10 Å. Kohn–Sham wave functions of the valence electrons were expanded in a plane wave basis with an energy cut-off of 450 eV. The Brillouin zone sampling was carried out using a Monkhorst Pack grid containing $3 \times 3 \times 1$ k-points. Ionic relaxation was performed using the conjugate-gradient method until the forces were reduced to values less than 0.02 eV $Å^{-1}$ for atoms with unconstrained freedom. We considered a supercell with $a = b = 10.60$ Å and $c = 17$ Å. The optimized crystal structure for the CoPt (1:1) alloy was found to have tetragonal $L1_0$ symmetry with the P4/mmm space group and with lattice constants of $a = 2.65$ Å and $c = 3.74$ Å, in which Co occupies the 1a (0,0,0) site and Pt occupies the 1d (0.5,0.5,0.5) site (Supplementary Figure S1). The (111) surface was constructed from this relaxed bulk structure (see Supplementary Figure S2a for the CoPt surface viewed along the crystallographic *c*-axis and Supplementary Figure S2b for the surface along the *b*-axis). The surface contains chains of Co and Pt atoms lying alternately in the *a*–*b* planes. The two bottom layers were fixed to their bulk positions while the two surface layers were allowed to relax. For the calculations of surfaces with ligands (either OH or NH_3), dipole correction was applied along the direction perpendicular to the metal surface.

RESULTS AND DISCUSSION

Electrochemically stable N-containing polymers such as PNIPAM were required because they needed to withstand low pH and high potentials during the ORR process in an acidic environment. Organic molecules are likely to detach from the surfaces of PtCo nanoparticles during electrochemical reactions if small organic molecules with short chain lengths are directly adsorbed without any anchoring site on the carbon surfaces for PtCo surface modification. Therefore, to covalently combine PNIPAM with the Vulcan carbon surface, C-PNIPAM was fabricated by an amide reaction between –COOH, a surface functional group on the carbon black and the $–NH_2$ of the amine-terminated PNIPAM (NH_2-PNIPAM).[42] The $-NH_2$ groups of NH_2-PNIPAM served as bridge groups only to form anchoring sites between the carbon surface and PNIPAM. As shown in Supplementary Figure S3, the TGA curve of C-PNIPAM exhibited a ~ 4 wt.% loss between 300 and 400 °C, while that of pristine carbon without PNIPAM hardly changed in the same temperature region. However, both of the carbon materials with and without PNIPAM were burned out at a similar temperature between 600 and 750 °C. Therefore, we could conclude that the carbon surface of C-PNIPAM was functionalized with as much as ~ 4 wt.% PNIPAM, based on the TGA curves of different kinds of carbon materials.[43,44] Pt and Co precursors were homogeneously mixed in a C-PNIPAM-dispersed solvent and then rapidly reduced to the metal nanoparticles by $NaBH_4$, which acted as the reducing agent. To clarify the effects of PNIPAM on the Co electronic structure, monometallic Pt and Co nanoparticles were also prepared using carbon with and without PNIPAM (that is, Pt/C-PNIPAM, Pt/C, Co/C-PNIPAM and Co/C as well as the traditional PtCo/C without PNIPAM). Prior to the nanoparticle synthesis, the interactions between the metal precursors and PNIPAM were confirmed by UV–Vis spectral measurements. Interestingly, as shown in Figure 2a, the spectra indicated that only the Co precursor interacted strongly with PNIPAM in the region between 400 and 800 nm (as demonstrated by the decrease in the absorption intensity in this region), although both the Pt and Co precursors were present with PNIPAM in the solvent. While the Pt precursor showed light absorbance between 300 and 400 nm, there was hardly any charge transfer between the Pt precursor and PNIPAM, because the absorption intensities of the two samples were very similar in the spectral region regardless of the presence of PNIPAM. The decrease in the light absorbance of the Co precursor indicated that the *d*-orbital of the Co ions was occupied by electrons transferred from PNIPAM to the Co^{2+} ion, which may be attributed to the formation of the Co^{2+}-PNIPAM complex. This hypochromism can be explained by the formation of metal complexes due to the ligand-to-metal charge transfer.[45,46] In addition, as shown in Supplementary Figure S4, when the Co precursor used to prepare the Co/C-PNIPAM was mixed with PNIPAM, it also exhibited hypo-

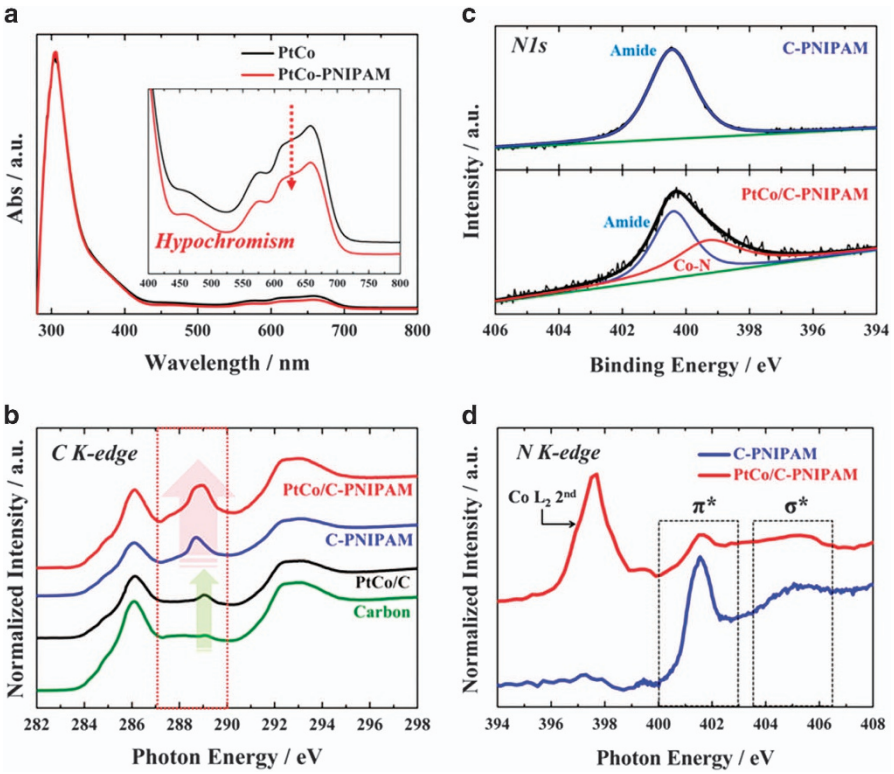

Figure 2 (**a**) UV–Vis absorption spectra of the solutions containing Pt and Co precursors with and without PNIPAM. The inset is the enlarged spectra in the wavelength region between 400 and 800 nm. (**b**) C K-edge NEXAFS spectra of bare carbon, PtCo/C, C-PNIPAM and PtCo/C-PNIPAM. (**c**) N 1*s* core-level XPS spectra and deconvoluted curves of C-PNIPAM (top) and PtCo/C-PNIPAM (bottom). In the deconvoluted XPS curves, blue, red and green lines indicate the amide N, Co–N and background peaks, respectively. (**d**) N K-edge NEXAFS spectra of C-PNIPAM and PtCo/C-PNIPAM. In the case of the N K-edge NEXAFS spectrum of PtCo/C-PNIPAM, the Co L_2 second harmonic is due to the existence of Co in the sample. NEXAFS, near-edge X-ray absorption fine structure; UV–Vis, ultraviolet–visible, XPS, X-ray photoelectron spectroscopy.

chromism due to the presence of PNIPAM, whereas the Pt precursor used for preparing for Pt/C-PNIPAM was not affected by PNIPAM as in the case of PtCo-PNIPAM, shown in Figure 2a. Therefore, only the Co precursor exhibited selective interaction with PNIPAM.

After the PtCo nanoparticle synthesis, the NEXAFS of carbons was measured to prove the PNIPAM functionalization on carbon and to study the interaction between the metal nanoparticles and the chemically attached PNIPAM on the carbon surfaces (Figure 2b). The C K-edge features between 287 and 290 eV generally appear as a result of various functional groups on the carbon surface.[47,48] In addition, the functionalization intensity in this region increases with the metal nanoparticle hybridization via the functional groups on the carbon surfaces.[47,48] As shown in Figure 2b, bare carbon without PNIPAM or metal nanoparticles showed a low intensity in the energy region between 287 and 290 eV. Subsequently, the intensity slightly increased owing to a small number of functional groups (–COOH, –COO, –CO and so on) on the carbon surface interacting with the PtCo nanoparticles after PtCo/C was synthesized. However, PNIPAM-functionalized C-PNIPAM had high functionalization intensity on its own due to the PNIPAM chemically attached to the carbon surface. In addition, PtCo/C-PNIPAM showed a much higher intensity in the energy region, which was attributed to the strong hybridization effects after the PtCo nanoparticle formation on C-PNIPAM.

Furthermore, as shown in Figure 2c and Supplementary Table S1, the metal-N bond formation was confirmed to be as high as ~48% of all the N contents in PNIPAM from N 1 s core-level XPS of PtCo/C-PNIPAM, while C-PNIPAM only exhibited an amide N peak as a result of the basic structure of PNIPAM.[49,50] As expected, N peaks were not present in the XPS spectra of bare carbon and PtCo/C, as shown in Supplementary Figure S5. However, metal-N bonds only formed in the case of Co/C-PNIPAM and not in Pt/C-PNIPAM, as shown in Supplementary Figure S6 and Supplementary Table S1. This implies that the interaction between Pt and PNIPAM was negligible compared with that between Co and PNIPAM. Therefore, based on the UV–Vis and XPS spectra, it is likely that Co–N bonds formed preferentially over Pt–N.

As shown in Figure 2d, the π^* absorption peak for the amide N (~401.5 eV) of PtCo/C-PNIPAM was significantly decreased compared with that of C-PNIPAM, which means that the amide N sites of PNIPAM may be used to form Co–N bonds on PtCo nanoparticles.[47,51,52] In addition, the σ^* absorption feature (~405 eV) of PtCo/C-PNIPAM broadened, and its intensity was reduced, which may be attributed to a geometrical change for the C–N bond from sp^2 to sp^3 configurations by the interaction between the surface Co on the PtCo nanoparticles and the amide N in the PNIPAM functionalized on the carbon surfaces.[47] In addition, as shown in Supplementary Figure S7, both PtCo/C-PNIPAM and PtCo/C showed similar patterns in the X-ray diffraction measurements related to their periodic bulk structures rather than their surface structures. Consequently, it may be concluded that PtCo alloy nanoparticles with Pt-(Co–N_{surf}) formed on the surfaces were successfully synthesized using C-PNIPAM as a support material.

However, as shown in Figures 3a and b, it was difficult to discern the morphological differences between PtCo/C-PNIPAM and PtCo/C samples in the TEM images. Therefore, to visually demonstrate the existence of Pt-(Co–N_{surf}) in PtCo/C-PNIPAM, energy-dispersive

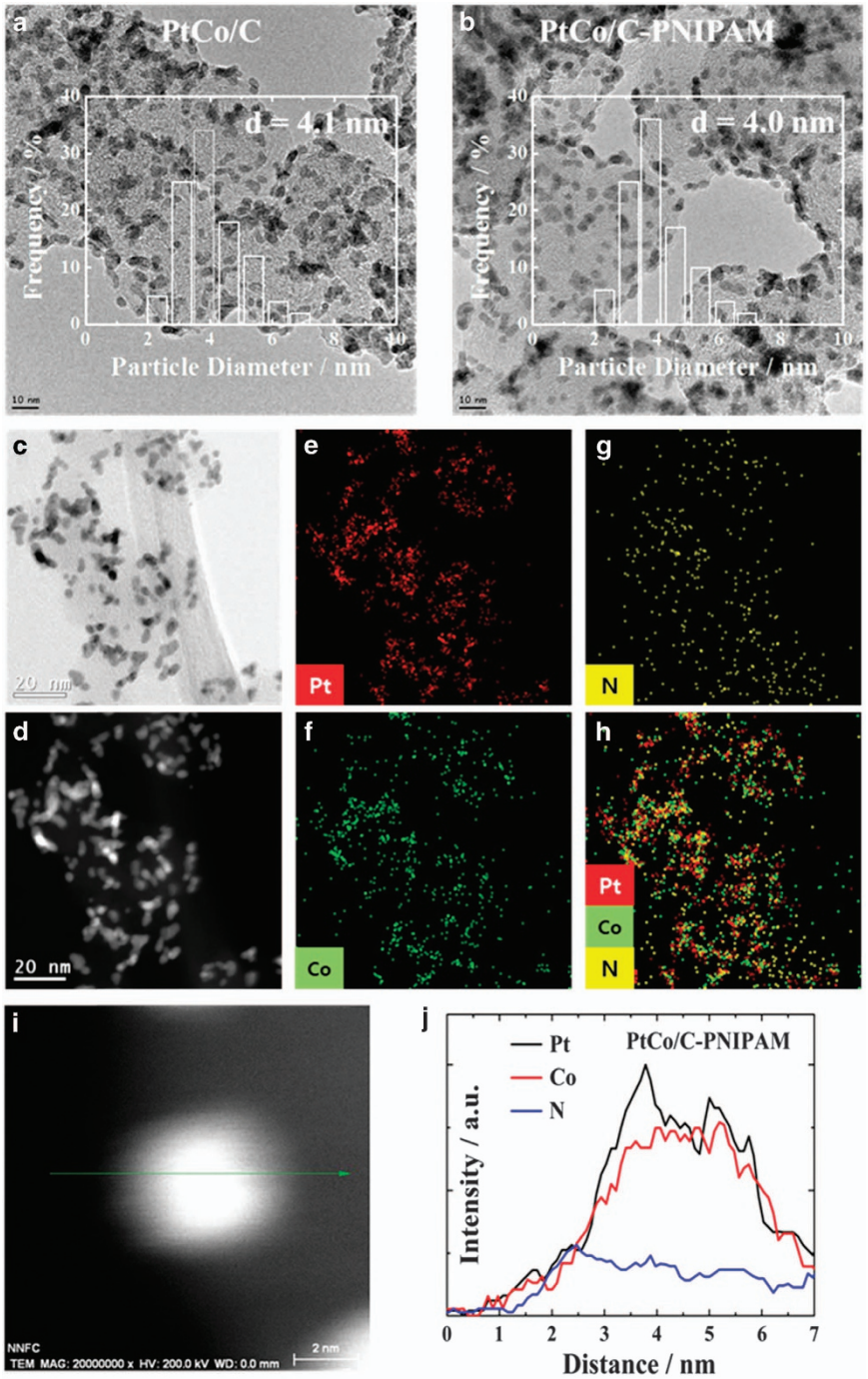

Figure 3 TEM images overlayed with particle size distributions of as-prepared (**a**) PtCo/C and (**b**) PtCo/C-PNIPAM. (**c**) Bright-field and (**d**) dark-field STEM images of PtCo/C-PNIPAM at low magnification. Energy-dispersive X-ray spectroscopy elemental mapping images for (**e**) Pt, (**f**) Co and (**g**) N and (**h**) the overlapped mapping image with all the elements in the same region of the PtCo/C-PNIPAM sample. (**i**) Dark-field STEM image of a nanoparticle scanned along the direction of the green arrow and (**j**) the resultant line profile of Pt, Co and N in PtCo/C-PNIPAM sample. STEM, scanning transmission electron microscope.

X-ray spectroscopy mapping and line scanning measurements were performed for the PtCo/C-PNIPAM samples using a Cs-corrected STEM. As shown in Figures 3c–h, the N element in the amide functional groups of PNIPAM was detected mainly on the surface of the PtCo nanoparticles and not on the bare carbon surface. In addition, the co-existence of Pt, Co and N atoms was clearly identified from the line profile of PtCo/C-PNIPAM in Figures 3i and j. However, it was still difficult to precisely observe the selective PNIPAM functionalization on the surface Co atoms of the modified PtCo nanoparticles by the TEM measurements because of the physical limitation of TEM resolution. Therefore, we needed to closely study the electronic and chemical structure changes of Co and Pt with various X-ray spectroscopy methods such as NEXAFS, XANES and XPS to prove the effects of PNIPAM on PtCo nanoparticles.

Before the Pt-(Co–N_{surf}) surfaces are formed on C-PNIPAM, the Co precursors may have an excess of electrons due to their strong

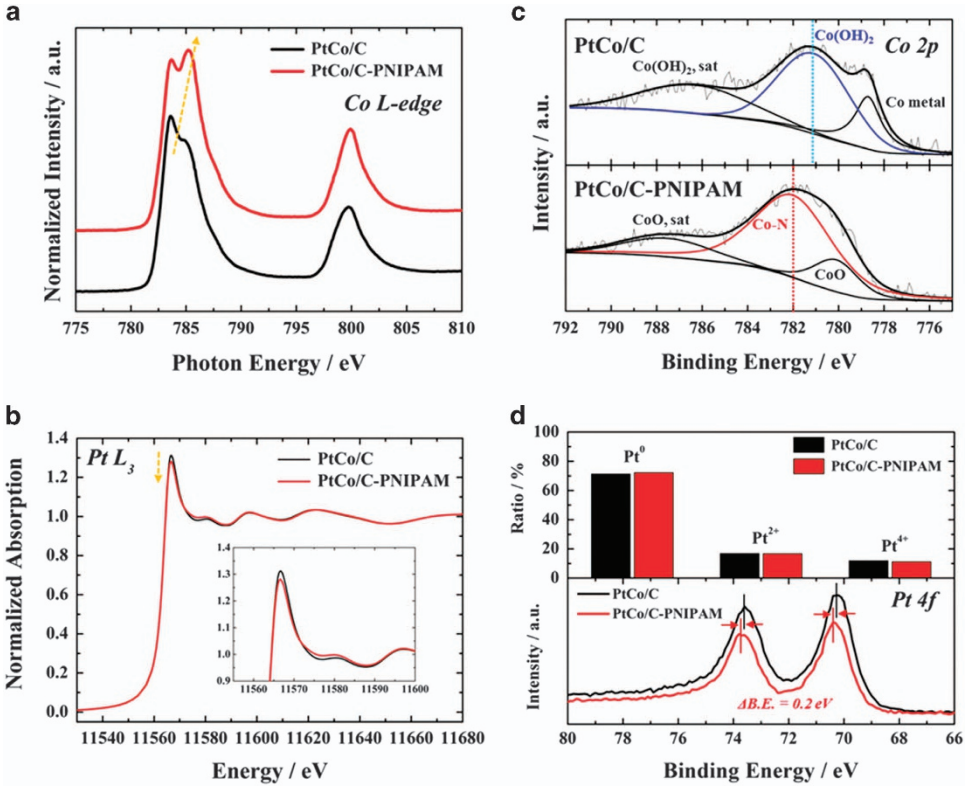

Figure 4 Co and Pt electronic structures in catalysts. (**a**) Co L-edge NEXAFS and (**b**) Pt L_3-edge XANES spectra of PtCo/C and PtCo/C-PNIPAM. The inset in **b** is an enlargement of the white line absorption region. Dotted yellow arrows indicate the change of the spectra. (**c**) Deconvoluted Co 2p core-level XPS spectra. (**d**) The ratios of Pt oxidation states (top) and Pt 4f core-level XPS spectra (bottom) of PtCo/C and PtCo/C-PNIPAM. ΔB.E. indicates the difference in binding energies between the main peaks. NEXAFS, near-edge X-ray absorption fine structure; XPS, X-ray photoelectron spectroscopy.

interaction with PNIPAM, which donates the electrons, as shown in Figure 2a. However, once the Pt-(Co–N_{surf}) surfaces were formed by a strong reducing agent, the extra electrons in the surface Co atoms were expected to transfer instantly to the *d*-orbitals of the surface Pt atoms, owing to the increase in the electronegativity difference between Pt and Co. In fact, as shown in Figure 4, the electronic structures of Co and Pt in PtCo/C-PNIPAM changed dramatically as a result of the interactions with PNIPAM. The Co L-edge NEXAFS and Pt L_3-edge XANES spectra shown in Figures 4a and b, respectively, confirmed that the *d*-orbital in the Co atoms lost more electrons and that the number of Pt *d*-band vacancies was lower in PtCo/C-PNIPAM than in PtCo/C. In general, as Co has a higher oxidation state (that is, it loses more electrons), Co L-edge absorption peaks are positively shifted because a higher energy is required to excite the 2*p* electrons strongly bounded to the less-screened nucleus.[47,53,54] In this study, the more positive shift of the absorption peaks in Co L_3-edge NEXAFS of PtCo/C-PNIPAM means that Co lost more 3*d* electrons in PtCo/C-PNIPAM than in PtCo/C, and the electrons were transferred to Pt (as indicated by a decrease in the white line intensity of Pt L_3-edge XANES) in PtCo/C-PNIPAM. This implies that the electron transfer from Co to Pt was significantly enhanced in PtCo/C-PNIPAM, which can be confirmed by investigating the changes in the electronic structure of the other samples. As expected from the UV–Vis spectra, in the cases of Pt/C-PNIPAM and Pt/C, the Pt electronic structures were completely identical to the results obtained from the Pt L_3-edge XANES spectra, shown in Supplementary Figure S8a. In sharp contrast, as shown in Supplementary Figure S8b, the absorption intensity of Co/C-PNIPAM was higher in the low energy region than that of Co/C, implying that Co/C-PNIPAM could have higher *d*-orbital filling than Co/C owing to the absence of more electronegative hetero metal atoms such as Pt that could receive the excess electrons from the Co atoms. Therefore, the explanation for the enhanced electron transfer in PtCo/C-PNIPAM was considered to be appropriate.

In terms of the chemical structure, as shown in the Co 2p XPS spectra in Figure 4c, the Co–N peak at 782.0 eV indicated the presence of Co–N on the surface of PtCo/C-PNIPAM,[49,50,55] whereas PtCo/C showed peaks at 781.1 eV and 778.8 eV, which are attributed to Co $(OH)_2$ and metallic Co, respectively (Supplementary Table S2).[56] In addition, as shown in Figure 4d, the peaks in the Pt 4 f XPS spectra for PtCo/C-PNIPAM were shifted to binding energies 0.2 eV higher than those corresponding to PtCo/C, even though the oxidation states of Pt were similar in both catalysts (Supplementary Figure S9 and Supplementary Table S3). The features in the Pt 4 f XPS spectra for PtCo/C-PNIPAM indicated a downshift in the electronic structure at the core level, which ultimately involved a Pt *d*-band downshift.[57,58] Therefore, without physically blocking the active Pt surfaces, the Pt electronic structure was successfully modified by the electronic ensemble effect between Pt and Co–N_{surf} on the surface of the PtCo nanoparticles.

To study the electrochemical properties of PtCo nanoparticles containing Pt-(Co–N_{surf}) on the surface, the ORR polarization curves and CVs for PtCo/C-PNIPAM and PtCo/C were obtained before and after the ADT. The ADT included 5000 cycles between potentials of 0.6 V_{RHE} and 1.1 V_{RHE} in an O_2-saturated 0.1 M $HClO_4$ electrolyte. Before the electrochemical tests, the ORR activity of C-PNIPAM was confirmed to be very low but comparable to that of pristine carbon, as shown in Supplementary Figure S10. Therefore, the PNIPAM

functionalization rarely had an effect on the ORR activity of the carbon support material. While PtM alloy catalysts such as PtCo/C generally have much higher initial ORR activities than the Pt catalyst due to the electronic ligand effect of the electron transfer from the TM to Pt, they also rapidly degrade owing to the TM oxidation and dissolution.[5,26] The surface Pt can also be concomitantly oxidized owing to the collapse of its initial structure by the TM dissolution in the ADT.[59]

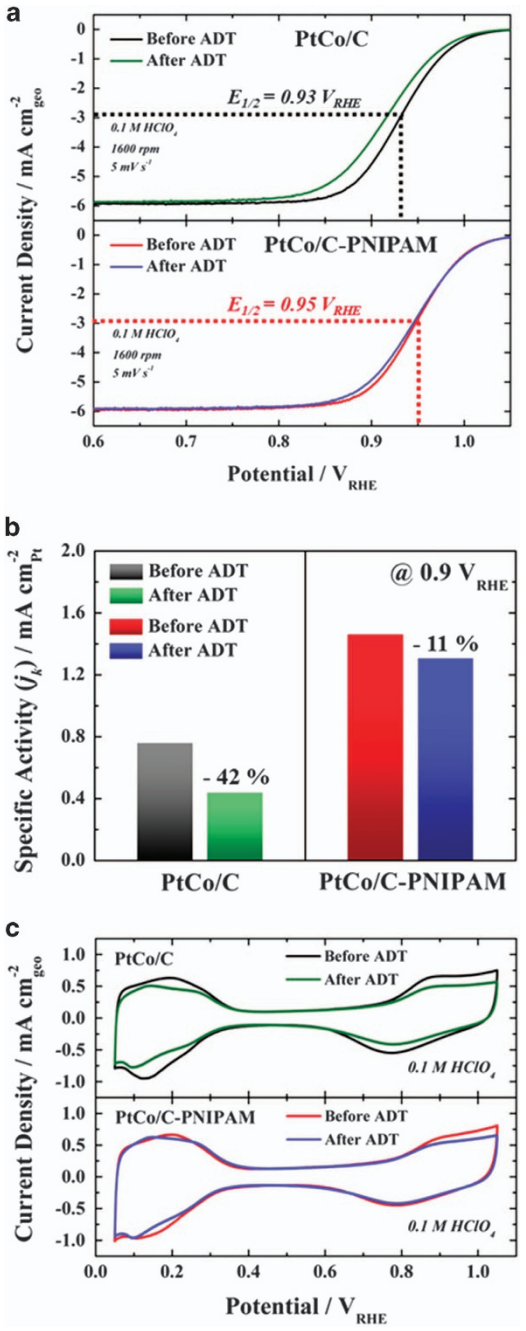

Figure 5 Electrochemical properties of catalysts before and after ADTs. The changes in (**a**) the ORR polarization curves ($E_{1/2}$ indicates the half-wave potential of the catalysts in the ORR polarization curves measured before the ADTs), (**b**) the specific activities at 0.9 V_{RHE} for the ORR, and (**c**) the CVs for PtCo/C and PtCo/C-PNIPAM before and after the ADTs. ADT, accelerated durability test; CV, Cyclic voltammogram; ORR, oxygen reduction reaction.

As expected, both PtCo/C and PtCo/C-PNIPAM had much higher ORR activities compared with Pt/C (Supplementary Figure S11). However, as shown in Figures 5a and b, PtCo/C-PNIPAM showed superior ORR activity and durability than PtCo/C. The initial ORR activity of PtCo/C-PNIPAM was considerably enhanced over that of PtCo/C owing to the Pt *d*-band downshift as a result of the electronic ensemble effect between Pt and Co–N_{surf}, as mentioned above. The half-wave potential ($E_{1/2}$) of PtCo/C-PNIPAM (0.95 V_{RHE}) was 20 mV higher than that of PtCo/C (0.93 V_{RHE}) before the ADTs. In addition, the specific activity of PtCo/C-PNIPAM containing surface Co–N bonds (which was ~11% lower) could be maintained even after the harsh ADT, whereas that of PtCo/C without PNIPAM was significantly degraded by ~42%. The excellent performance of PtCo/C-PNIPAM containing surface Co–N bonds could be attributed to the N attached to the Co sites on the PtCo nanoparticle surface, which prevents the further oxidation of the surface Co atoms by external O species such as O_2 gas, H_2O, OH_{ad} and so on This can be indirectly inferred from the lower ORR activity of Co/C-PNIPAM compared with that of Co/C in 0.1 M KOH, as shown in Supplementary Figure S12a. The surface Co atoms in Co/C are used as active materials for the ORR in KOH because they can withstand dissolution in alkaline solutions. However, the surface Co atoms in Co/C-PNIPAM were unable to react sufficiently with the O_2 gas in the electrolyte because some of the active surface Co sites were blocked by the N moieties due to the surface Co–N bond formation. On the other hand, Pt/C-PNIPAM and Pt/C showed almost the same ORR activities in O_2-saturated 0.1 M $HClO_4$ because the Pt was not affected by PNIPAM (Supplementary Figure S12b).

Furthermore, as shown in Figure 5c and Supplementary Table S4, PtCo/C-PNIPAM and PtCo/C had similar electrochemical surface areas before the ADT because the active surface Pt atoms were physically intact during the selective Co–N bond formation in PtCo/C-PNIPAM. However, after the ADT, although the electrochemical surface area of PtCo/C was significantly reduced by 23.6%, that of PtCo/C-PNIPAM was only slightly decreased by 3.1% because of the electrochemical stability of the Co–N bonds in the proximity of Pt. As shown in Figure 6, PtCo nanoparticles on the PtCo/C after the ADT agglomerated together into larger particles with irregular shapes compared with those before the ADT. In sharp contrast, the particle morphology of PtCo/C-PNIPAM changed very little and was found to be quite stable even after the ADT. It was hypothesized that the N moiety on the surface Co atoms could prevent oxidative O species from accessing the Co atoms. The oxidation and dissolution of Pt were also inhibited because the O-binding energy of Pt decreased owing to the Pt *d*-band downshift in PtCo/C-PNIPAM. Consequently, by exploiting the surface ensemble effects as a result of the selective Co–N_{surf} formation near the surface Pt atoms, we were able to indirectly tailor the Pt electronic structure to enhance the ORR activity and simultaneously suppress the degradation of the catalytic activity of PtCo nanoparticles.

To clearly explain the electronic ensemble effect, DFT calculations were conducted for the modified PtCo alloy surfaces. We considered the NH_3-adsorbed PtCo surface as a model system for simulating the Pt-(Co–N_{surf}) surface structure of the PtCo/C-PNIPAM catalyst. First, we found that the on-top site is most energetically favorable for NH_3-adsorption on the (111) surfaces of either pure Co/Pt or the PtCo alloy. In the case of the PtCo alloy surface, the calculated adsorption energies of NH_3 attached to Co and Pt were 0.80 eV and 0.66 eV, respectively, showing that NH_3 adsorption occurs preferentially on the Co sites rather than the Pt sites. After obtaining the basic surface structures, we determined the number of extra electrons per Pt ion at the surface (topmost layer) using Bader

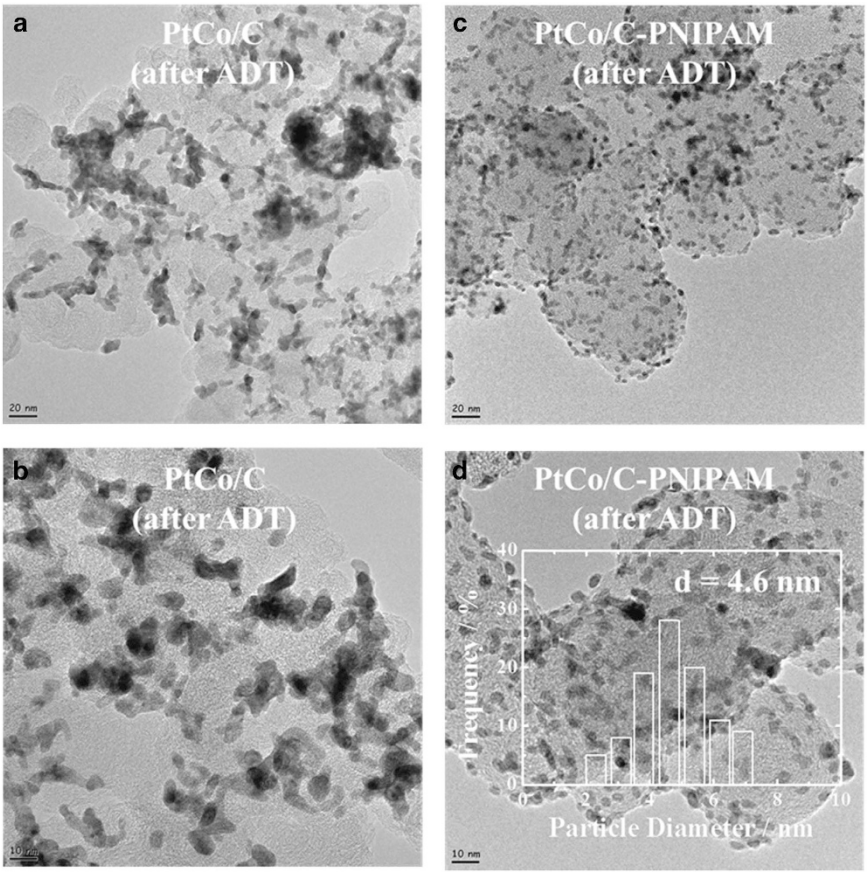

Figure 6 TEM images of (**a** and **b**) PtCo/C and (**c** and **d**) PtCo/C-PNIPAM after the ADTs. The size distribution and average diameter ($d = 4.6$ nm) of PtCo nanoparticles in PtCo/C-PNIPAM were indicated in (**d**). However, the PtCo particle size in PtCo/C could not be defined due to the irregular particle shapes after the ADT. ADT, accelerated durability test; TEM, transmission electron microscope.

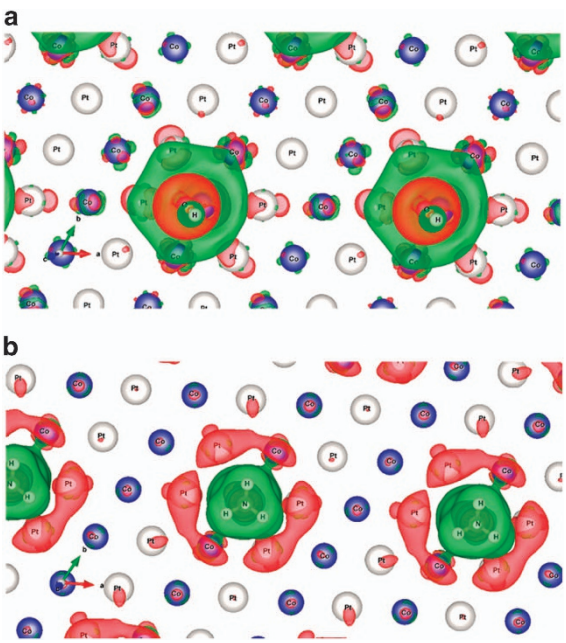

Figure 7 Simulated electronic structures of PtCo surfaces saturated with (**a**) OH and (**b**) NH_3. The electron distributions changed considerably on the PtCo surfaces when OH or NH_3 was adsorbed onto the surfaces. Red and green indicate the electron gain and loss, respectively.

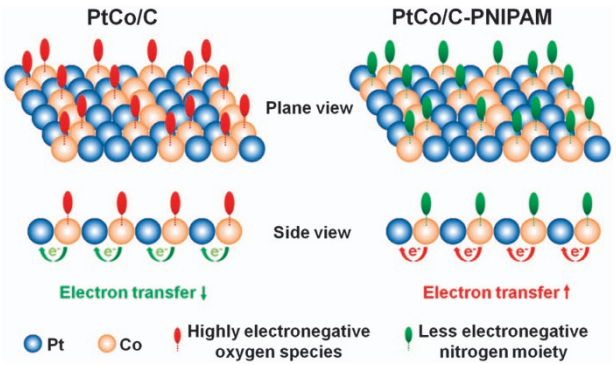

Figure 8 Schematic diagram of the electronic ensemble effect selectively tailoring the surface Co atoms in top sites with the N moiety on the PtCo nanoparticle surface.

analysis[60] for three different cases, namely (a) a pure PtCo surface, (b) a PtCo surface saturated with OH, and (c) a PtCo surface saturated with NH_3. For case c, the ligand ($–NH_3$) is attached to the TM site, whereas in case b, the ligand (–OH) is attached to the fcc-hollow site, to which OH binds strongly. All the estimates of the number of extra electrons are relative to the number of electrons in a Pt atom at the pure Pt (111) surface. The number of extra electrons per Pt atom was determined to be 0.5, 0.4 and 0.6 for the pure PtCo surface, the PtCo surface saturated with OH and the PtCo surface saturated with NH_3,

respectively. This clearly demonstrates that the presence of a more weakly electronegative element such as N in the ligand leads to enhanced electron transfer from Co to Pt, as shown in Figure 7, which is consistent with the changes in the electronic structures of the prepared catalysts shown in Figure 4.

To confirm the electrochemical stability of the Co atoms at the surface, we calculated the vacancy formation energies of Co in a bare PtCo surface, Co-OH in a PtCo surface saturated with OH and Co–NH_3 in a PtCo surface saturated with NH_3. The vacancy formation energies for the three cases were 5.40 eV, 6.25 eV and 8.01 eV, respectively, which shows that the oxidation and dissolution of Co in aqueous electrolytes can be significantly reduced by the electronic ensemble effect via NH_3 treatment. We also determined the Pt–O adsorption energies for different surfaces to investigate the relationship between the surface structures and the electrochemical durability of the catalysts because the adsorption energy is closely related to the oxidation and degradation of the Pt surface during the ORR under acidic conditions. For a general PtCo surface saturated with OH, the Pt–O adsorption energy was 0.590 eV due to the occupation of excess OH, whereas that of a bare PtCo surface was 3.385 eV. However, in terms of the surface oxidation state, it is difficult to accept the simulated result of the Pt–O adsorption energy for a PtCo surface saturated with OH, because the surface Pt atoms, which are already occupied by OH on the fcc-hollow site, may be electrochemically unstable. Therefore, to obtain meaningful results, the Pt–O adsorption energy of NH_3-saturated PtCo should be compared with those of bare PtCo (3.385 eV) and pure Pt (4.490 eV) surfaces. Consequently, the Pt–O adsorption energy for PtCo saturated with NH_3 was significantly reduced to 2.890 eV as a result of the Co–N_{surf} formation. These results indicate that the oxidation and/or dissolution of Pt can also be considerably retarded by the surface passivation of Co by N ligands. Therefore, the selective interaction of a TM with NH_3 helps not only in the process of charge transfer from TMs to Pt but also in reducing the dissolution and oxidation of the surface Pt and TM atoms. Therefore, our calculations clearly demonstrated that the surface ensemble effects between Pt and the surrounding Co–N tailor the electronic structure of Pt in a manner that enhances the ORR activity and the durability of the system, as shown in Figure 8.

CONCLUSIONS

We have proposed a new synthesis strategy to selectively attach a less electronegative N moiety to the surface Co atoms (the Co–N_{surf} formation) to simultaneously enhance electron transfer from Co to Pt and prevent the oxidation of Co atoms on PtCo nanoparticle surfaces. Carbon functionalized with a polymer containing amide groups (N moieties), C-PNIPAM, was used as a support material instead of bare carbon black. PNIPAM selectively and strongly interacted with the Co precursor, which resulted in the formation of Co–N_{surf} on the PtCo nanoparticles without affecting the surface Pt atoms. As a result, in PtCo/C-PNIPAM, the electron transfer from Co to Pt was considerably enhanced owing to an increase in the electronegativity difference between Pt and Co atoms. Thanks to the electronic ensemble effects between Pt and Co–N_{surf}, the ORR activity was significantly increased. PtCo/C-PNIPAM also showed much higher durability during the ADT because the Co–N_{surf} formation hindered the access of the O species to the Co atoms, and the Pt *d*-band was filled by excess electrons transferred from Co. The synthesis strategy for PtCo nanoparticles proposed in this study involving the use of C-PNIPAM as a support material is unique because the electronic structure of the active surface Pt can be indirectly tailored by selectively modifying the TM surface during the PtM alloy synthesis. The proposed organic/inorganic hybrid concept will also provide new insights into the tuning of nanomaterials consisting of heterogeneous metallic elements for various electrochemical and chemical applications.

CONFLICT OF INTEREST

The authors declare no conflict of interest.

ACKNOWLEDGEMENTS

This work was supported by the Global Frontier R&D Program at the Center for Multiscale Energy Systems funded by the National Research Foundation (NRF), Korea (2012M3A6A7054283) and supported by an NRF grant funded by MSIP, Korea (2014R1A2A2A04003865) and by the New & Renewable Energy Core Technology Program of KETEP grant funded by MOTIE, Korea (20133030011320). This work (S-CL) was partly supported by the Convergence Agenda Program (CAP) of the Korea Research Council of Fundamental Science and Technology (KRCF) and by the Nano Material Technology Development Program through the NRF funded by the Ministry of Education, Science, and Technology (No. 2013043467).

Author contributions: NJ conceived the idea, performed the experiments and wrote the manuscript. SB, UVW and S-CL simulated the PtCo surfaces with DFT calculations and wrote the computational simulation section of the manuscript. SG and K-HC measured and analyzed the NEXAFS of C, N and Co in the catalysts. H-YP, JR and Y-HC measured the XANES of Pt in the catalysts. S-YL, IJ and JHJ constructed the experimental setup. SHP, DYC and Y-ES contributed to discussions of the electrochemical data. S-CL and SJY coordinated and supervised the overall project. All authors reviewed the final manuscript.

1 Stamenkovic, V. R., Mun, B. S., Arenz, M., Mayrhofer, K. J. J., Lucas, C. A., Wang, G., Ross, P. N. & Markovic, N. M. Trends in electrocatalysis on extended and nanoscale Pt-bimetallic alloy surfaces. *Nat. Mater.* **6**, 241–247 (2007).
2 Debe, M. K. Electrocatalyst approaches and challenges for automotive fuel cells. *Nature* **486**, 43–51 (2012).
3 Cui, C., Gan, L., Heggen, M., Rudi, S. & Strasser, P. Compositional segregation in shaped Pt alloy nanoparticles and their structural behavior during electrocatalysis. *Nat. Mater.* **12**, 765–771 (2013).
4 Gasteiger, H. A. & Markovic, N. M. Just a dream-or future reality? *Science* **324**, 48–49 (2009).
5 Greeley, J., Stephens, I. E. L., Bondarenko, A. S., Johansson, T. P., Hansen, H. A., Jaramillo, T. F., Rossmeisl, J., Chorkendorff, I. & Norskov, J. K. Alloys of platinum and early transition metals as oxygen reduction electrocatalysts. *Nat. Chem.* **1**, 552–556 (2009).
6 Cho, Y.-H., Park, H.-S., Cho, Y.-H., Jung, D.-S., Park, H.-Y. & Sung, Y.-E. Effect of platinum amount in carbon supported platinum catalyst on performance of polymer electrolyte membrane fuel cell. *J. Power Sources* **172**, 89–93 (2007).
7 Lim, J. W., Cho, Y.-H., Ahn, M., Chung, D. Y., Cho, Y.-H., Jung, N., Kang, Y. S., Kim, O.-H., Lee, M. J., Kim, M. & Sung, Y.-E. Ionic resistance of a cathode catalyst layer with various thicknesses by electrochemical impedance spectroscopy for PEMFC. *J. Electrochem. Soc.* **159**, B378–B384 (2012).
8 Cui, C., Gan, L., Li, H.-H., Yu, S.-H., Heggen, M. & Strasser, P. Octahedral PtNi nanoparticle catalysts: exceptional oxygen reduction activity by tuning the alloy particle surface composition. *Nano Lett.* **12**, 5885–5889 (2012).
9 Wang, C., Chi, M, Wang, G., Vliet, D., Li, D., More, K., Wang, H.-H., Schlueter, J. A., Markovic, N. M. & Stamenkovic, V. R. Correlation between surface chemistry and electrocatalytic properties of monodisperse PtxNi1-x nanoparticles. *Adv. Funct. Mater.* **21**, 147–152 (2011).
10 Guo, S., Zhang, S. & Sun, S. Tuning nanoparticle catalysis for the oxygen reduction reaction. *Angew. Chem. Int. Ed.* **52**, 8526–8544 (2013).
11 Bing, Y., Liu, H., Zhang, L., Ghosh, D. & Zhang, J. Nanostructured Pt-alloy electrocatalysts for PEM fuel cell oxygen reduction reaction. *Chem. Soc. Rev.* **39**, 2184–2202 (2010).
12 Stephens, I. E. L., Bondarenko, A. S., Gronbjerg, U., Rossmeisl, J. & Chorkendorff, I. Understanding the electrocatalysis of oxygen reduction on platinum and its alloys. *Energy Environ. Sci.* **5**, 6744–6762 (2012).
13 Xu, Y., Ruban, A. V. & Mavrikakis, M. Adsorption and dissociation of O2 on Pt-Co and Pt-Fe alloys. *J. Am. Chem. Soc.* **126**, 4717–4725 (2004).
14 Bhattacharjee, S., Gupta, K., Jung, N., Yoo, S. J., Waghmare, U. V. & Lee, S.-C. Site preference of NH3-adsorption on Co, Pt and CoPt surfaces: the role of charge transfer, magnetism and strain. *Phys. Chem. Chem. Phys.* **17**, 9335–9340 (2015).
15 Guo, S., Li, D., Zhu, H., Zhang, S., Markovic, N. M., Stamenkovic, V. R. & Sun, S. FePt and CoPt nanowires as efficient catalysts for the oxygen reduction reaction. *Angew. Chem. Int. Ed.* **52**, 3465–3468 (2013).

16 Stamenkovic, V. R., Mun, B. S., Mayrhofer, K. J. J., Ross, P. N. & Markovic, N. M. Effect of surface composition on electronic structure, stability, and electrocatalytic properties of Pt-transition metal alloys: Pt-skin versus Pt-skeleton surfaces. *J. Am. Chem. Soc.* **128**, 8813–8819 (2006).
17 Hwang, S. J., Kim, S.-K., Lee, J.-G., Lee, S.-C., Jang, J. H., Kim, P., Lim, T.-H., Sung, Y.-E. & Yoo, S. J. Role of electronic perturbation in stability and activity of Pt-based alloy nanocatalysts for oxygen reduction. *J. Am. Chem. Soc.* **134**, 19508–19511 (2012).
18 Zhang, J., Yang, H., Fang, J. & Zou, S. Synthesis and oxygen reduction activity of shape-controlled Pt3Ni nanopolyhedra. *Nano Lett.* **10**, 638–644 (2010).
19 Stamenkovic, V., Mun, B. S., Mayrhofer, K. J. J., Markovic, N. M., Rossmeisl, J., Greely, J. & Norskov, J. K. Changing activity of electrocatalysts for oxygen reduction by tuning the surface electronic structure. *Angew. Chem. Int. Ed.* **45**, 2897–2901 (2006).
20 Strasser, P., Koh, S., Anniyev, T., Greely, J., More, K., Yu, C., Liu, Z., Kaya, S., Nordlund, D., Ogasawara, H., Toney, M. F. & Nilsson, A. Lattice-strain control of the activity in dealloyed core-shell fuel cell catalysts. *Nat. Chem.* **2**, 454–460 (2010).
21 Callejas-Tovar, R., Liao, W., Mera, H. & Balbuena, P. B. Molecular dynamics simulations of surface oxidation on Pt and Pt/PtCo/Pt3Co nanoparticles supported over carbon. *J. Phys. Chem. C* **115**, 23768–23777 (2011).
22 Ahmadi, M., Behafarid, F., Cui, C., Strasser, P. & Cuenya, B. R. Long-range segregation phenomena in shape-selected bimetallic nanoparticles: chemical state effects. *ACS Nano* **7**, 9195–9204 (2013).
23 Duong, H. T., Rigsby, M. A., Zhou, W.-P. & Wieckowski, A. Oxygen reduction catalysis of the Pt3Co alloy in alkaline and acidic media studied by X-ray photoelectron spectroscopy and electrochemical methods. *J. Phys. Chem. C* **111**, 13460–13465 (2007).
24 Jeon, T.-Y., Yoo, S. J., Cho, Y.-H., Lee, K.-S., Kang, S. H. & Sung, Y.-E. Influence of oxide on the oxygen reduction reaction of carbon-supported Pt-Ni alloy nanoparticles. *J. Phys. Chem. C* **113**, 19732–19739 (2009).
25 Antolini, E., Salgado, J. R. C. & Gonzalez, E. R. The stability of Pt-M (M=first row transition metal) alloy catalysts and its effect on the activity in low temperature fuel cells. A literature review and tests on a Pt-Co catalyst. *J. Power Sources* **160**, 957–968 (2006).
26 Gan, L., Heggen, M., O'Malley, R., Theobald, B. & Strasser, P. Understanding and controlling nanoporosity formation for improving the stability of bimetallic fuel cell catalysts. *Nano Lett.* **13**, 1131–1138 (2013).
27 Mayrhofer, K. J. J., Hartl, K., Juhart, V. & Arenz, M. Degradation of carbon-supoorted Pt bimetallic nanoparticles by surface segregation. *J. Am. Chem. Soc.* **131**, 16348–16349 (2009).
28 Oezaslan, M., Hasche, F. & Strasser, P. Oxygen electroreduction on PtCo3, PtCo and Pt3Co alloy nanoparticles for alkaline and acidic PEM fuel cells. *J. Electrochem. Soc.* **159**, B394–B405 (2012).
29 Stamenkovic, V. R., Fowler, B., Mun, B. S., Wang, G., Ross, P. N., Lucas, C. A. & Markovic, N. M. Improved oxygen reduction activity on Pt3Ni(111) via increased surface site availability. *Science* **315**, 493–497 (2007).
30 Wang, C., Chi, M., Li, D., Strmcnik, D., Vliet, D., Wang, G., Komanicky, V., Chang, K.-C., Paulikas, A. P., Tripkovic, D., Pearson, J., More, K. L., Markovic, N. M. & Stamenkovic, V. R. Design and synthesis of bimetallic electrocatalyst with multilayered Pt-skin surfaces. *J. Am. Chem. Soc.* **133**, 14396–14403 (2011).
31 Gan, L., Rudi, S. & Strasser, P. Core-shell compositional fine structures of dealloying PtxNi1-x nanoparticles and their impact on oxygen reduction catalysis. *Nano Lett.* **12**, 5423–5430 (2012).
32 Wang, D., Yu, Y., Xin, H. L., Hovden, R., Ercius, P., Mundy, J. A., Chen, H., Richard, J. H., Muller, D. A., DiSalvo, F. J. & Abruna, H. D. Tuning oxygen reduction reaction activity via controllable dealloying: a model study of ordered Cu3Pt/C intermetallic nanocatalysts. *Nano Lett.* **12**, 5230–5238 (2012).
33 Chen, S., Ferreira, P. J., Sheng, W., Yabuuchi, N., Allard, L. F. & Shao-Horn, Y. Enhanced activity for oxygen reduction reaction on "Pt3Co" nanoparticles: direct evidence of percolated and sandwich-segregation structures. *J. Am. Chem. Soc.* **130**, 13818–13819 (2008).
34 Jung, N., Chung, Y.-H., Chung, D. Y., Choi, K.-H., Park, H.-Y., Ryu, J., Lee, S.-Y., Kim, M., Sung, Y.-E. & Yoo, S. J. Chemical tuning of electrochemical properties of Pt-skin surfaces for highly active oxygen reduction reactions. *Phys. Chem. Chem. Phys.* **15**, 17079–17083 (2013).
35 Quarto, F. D., Sunseri, C., Piazza, S. & Romano, M. C. Semiempirical correlation between optical band gap values of oxides and the difference of electronegativity of the elements. Its importance for a quantitative use of photocurrent spectroscopy in corrosion studies. *J. Phys. Chem. B* **101**, 2519–2525 (1997).
36 Biesinger, M. C., Lau, L. W. M., Gerson, A. R. & Smart, R. St. C. The role of the Auger parameter in XPS studies of nickel metal, halides and oxides. *Phys. Chem. Chem. Phys.* **14**, 2434–2442 (2012).
37 Ferrando, R., Jellinek, J. & Johnston, R. L. Nanoalloys: from theory to applications of alloy clusters and nanoparticles. *Chem. Rev.* **108**, 845–910 (2008).
38 Lee, K.-S., Koo, H.-J., Dai, D., Ren, J. & Whangbo, M.-H. Electron counting scheme relevant for late transition metal compounds with weakly electronegative ligands. Electronic band structure study of phophosilicides PtSi3P2 and NiSi2P3. *Inorg. Chem.* **38**, 340–345 (1999).
39 Byers, W., Chou, B. F.-C., Lever, A. B. P. & Parish, R. V. Charge-transfer spectra of pyridine N-oxide metal complexes. Determination of optical electronegativities. *J. Am. Chem. Soc.* **91**, 1329–1333 (1969).
40 Kresse, G. & Furthmuller, J. Efficient iterative schemes for ab initio total-energy calculations using a plane-wave basis set. *Phys. Rev. B* **54**, 11169–11186 (1996).
41 Tang, W., Sanville, E. & Henkelman, G. A grid-based Bader analysis algorithm without lattice bias. *J. Phys.: Condens. Matter* **21**, 084204 (2009).
42 Jung, N., Kim, S. M., Kang, D. H., Chung, D. Y., Kang, Y. S., Chung, Y.-H., Choi, Y. W., Pang, C., Suh, K.-Y. & Sung, Y.-E. High-performance hybrid catalyst with selectively functionalized carbon by temperature-directed switchable polymer. *Chem. Mater.* **25**, 1526–1532 (2013).
43 Cao, L., Man, T., Zhuang, J. & Kruk, M. Poly(N-isopropylacrylamide) and poly(2-(dimethylamino)ethyl methacrylate) grafted on an ordered mesoporous silica surface using atom transfer radical polymerization with activators regenerated by electron transfer. *J. Mater. Chem.* **22**, 6939–6946 (2012).
44 Wu, T., Zhang, Q., Hu, J., Zhang, G. & Liu, S. Composite silica nanospheres covalently anchored with gold nanoparticles at the outer periphery of thermoresponsive polymer brushes. *J. Mater. Chem.* **22**, 5515–5163 (2012).
45 Srinivasan, S., Annaraj, J. & Athappan, P. R. Spectral and redox studies on mixed ligand complexes of cobalt(III) phenanthroline/bipyridyl and benzoylhydrazones, their DNA binding and antimicrobial activity. *J. Inorg. Biochem.* **99**, 876–882 (2005).
46 Pyle, A. M., Rehmann, J. P., Meshoyrer, R., Kumar, C. V., Turro, N. J. & Barton, J. K. Mixed-ligand complexes of ruthenium(II): factors governing binding to DNA. *J. Am. Chem. Soc.* **111**, 3051–3058 (1989).
47 Wang, J., Zhou, J., Hu, Y. & Regier, T. Chemical interaction and imaging of single Co3O4/graphene sheets studied by scanning transmission X-ray microscopy and X-ray absorption spectroscopy. *Energy Environ. Sci.* **6**, 926–934 (2013).
48 Liang, Y., Li, Y., Wang, H., Zhou, J., Wang, J., Regier, T. & Dai, H. Co3O4 nanocrystals on graphene as a synergistic catalyst for oxygen reduction reaction. *Nat. Mater.* **10**, 780–786 (2011).
49 Artyushkova, K., Pylypenko, S., Olson, T. S., Fulghum, J. E. & Atanassov, P. Predictive modeling of electrocatalyst structure based on structure-to-property correlation of X-ray photoelectron spectroscopic and electrochemical measurements. *Langmuir* **24**, 9082–9088 (2008).
50 Arechederra, R. L., Artyushkova, K., Atanassov, P. & Minteer, S. D. Growth of phthalocyanine dopedand undoped nanotubes using mild synthesis conditions for development of novel oxygen reduction catalysts. *ACS Appl. Mater. Interfaces* **2**, 3295–3302 (2010).
51 He, Q., Li, Q., Khene, S., Ren, X., Lopez-Suarez, F. E., Lozano-Castello, D., Bueno-Lopez, A. & Wu, G. High-;oading cobalt oxide coupled with nitrogen-doped graphene for oxtgen reduction in anion-exchange-membrane alkaline fuel cells. *J. Phys. Chem. C* **117**, 8697–8707 (2013).
52 Leinweber, P., Kruse, J., Walley, F. L., Gillespie, A., Eckhardt, K.-U., Blyth, R. I. R. & Regier, T. Nitrogen K-edge XANES—an overview of reference compounds used to identify 'unknown' organic nitrogen in environmental samples. *J. Syncrotron Rad.* **14**, 500–511 (2007).
53 Yoo, W.-S., Kim, K.-B., Kim, M.-G., Lee, M.-K., Shin, H.-J., Lee, J.-M., Lee, J.-S. & Yo, C.-H. Oxygen contribution on Li-ion intercalation-deintercalation in LiCoO2 investigated by O K-edge and Co L-edge X-ray absorption spectroscopy. *J. Phys. Chem. B* **106**, 2526–2532 (2002).
54 Yoon, W.-S., Grey, C. P., Balasubramanian, M., Yang, X.-Q. & McBreen, J. In situ X-ray absorption spectroscopic study on LiNi0.5Mn0.5O2 cathode material during electrochemical cycling. *Chem. Mater.* **15**, 3161–3169 (2003).
55 Morozan, A., Jegou, P., Jousselme, B. & Palacin, S. Electrochemical performance of annealed cobalt-benzotriazole/CNTs catalysts toward the oxygen reduction reaction. *Phys. Chem. Chem. Phys.* **13**, 21600–21607 (2011).
56 Tan, B. J., Klabunde, K. J. & Sherwood, P. M. A. XPS studies of solvated metal atom dispersed catalysts. Evidence for layered cobalt-manganese particles on alumina and silica. *J. Am. Chem. Soc.* **113**, 855–861 (1991).
57 Wakisaka, M., Mitsui, S., Hirose, Y., Kawashima, K., Uchida, H. & Watanabe, M. Electronic structures of Pt-Co and Pt-Ru alloys for CO-tolerant anode catalysts in polymer electrolyte fuel cells studied by EC-XPS. *J. Phys. Chem. B* **110**, 23489–23496 (2006).
58 Weinert, M. & Watson, R. E. Core-level shifts in bulk alloys and surface adlayers. *Phys. Rev. B* **51**, 17168–17180 (1995).
59 Huang, Y., Zhang, J., Kongkanand, A., Wagner, F. T., Li, J. C. M. & Jorne, J. Transient platinum oxide formation and oxygen reduction on carbon-supported platinum and platinum-cobalt alloy electrocatalysts. *J. Electrochem. Soc.* **161**, F10–F15 (2014).
60 Perdew, J. P., Burke, K. & Ernzerhof, M. Generalized gradient approximation made simple. *Phys. Rev. Lett.* **77**, 3865–3868 (1996).

Supplementary Information accompanies the paper on the NPG Asia Materials website (http://www.nature.com/am)